An Assessment of PET Dose Reduction with Penalized Likelihood Image Reconstruction using a Computationally Efficient Model Observer

Howard C. Gifford¹, C. Ross Schmidtlein², Andrzej Krol³, and Yuesheng Xu⁴

¹University of Houston, Houston, TX, USA

²Memorial Sloan Kettering Cancer Center, New York, NY, USA

³SUNY Upstate Medical University, Syracuse, NY, USA

⁴Old Dominion University, Norfolk, VA, USA

ABSTRACT

Developing PET reconstruction algorithms with improved low-count capabilities may provide a timely and cost-effective means of reducing radiation dose in promising clinical applications such as immuno-PET that require long-lived radiotracers. For many PET clinics, the reconstruction protocol consists of postsmoothed ordered-sets expectation-maximization (OSEM) reconstruction, but penalized likelihood methods based on total-variation (TV) regularization could substantially reduce dose. We performed a task-based comparison of postsmoothed OSEM and higher-order TV (HOTV) reconstructions using simulated images of a contrast-detail phantom. An anthropomorphic visual-search model observer read the images in a location-known receiver operating characteristic (ROC) format. Acquisition counts, target uptake, and target size were study variables, and the OSEM postfiltering was task-optimized based on count level. A psychometric analysis of observer performance for the selected task found that the HOTV algorithm allowed a two-fold reduction in dose compared to the optimized OSEM algorithm.

1. INTRODUCTION

Obtaining meaningful dose reductions in PET imaging requires improved hardware, tracer chemistry, and data processing. Advances in any of these areas will be synergistic with progress in the other areas. The largest reductions may come by improving the detector sensitivity of the imaging systems, but doing so can be quite expensive. Furthermore, some promising PET protocols, like immuno-PET applications involving monoclonal antibodies, are constrained by the need for long-lived, high-energy radioisotopes such as Zr-89. In these cases, there are physiological limits on sensitivity due to slow tracer uptake, and the possibility of using shorter-lived positron emitters appears to be some years away. Developing reconstruction algorithms with improved low-count capabilities could provide a timely and cost-effective means of realizing the potential of immumo-PET.

For many PET clinics, the reconstruction protocol consists of postsmoothed OSEM. One approach being tested for better low-count performance combines data deblurring and denoising within penalized likelihood methods. Total-variation (TV) regularization uses image gradients to reduce noise while preserving edges, but can create false positives through the introduction of staircasing artifacts. Alternatively, the use of higher-order gradients (higher-order TV, or HOTV) has been proposed to suppress these artifacts. In this paper, we discuss a simulation assessment of the OSEM and HOTV algorithms for target detection with varying acquisition counts. Our study made use of a visual-search (VS) model observer⁸ to generate psychometric data for comparing the low-count performance of the HOTV and OSEM algorithms.

Further author information: E-mail: hgifford@uh.edu

2. METHODS

2.1 Data Acquisition

The imaging simulation was carried out with a pair of discretized 3D mathematical phantoms (Fig. 1), each consisting of 47 256×256 transverse slices with a 3.3-mm slice thickness and a pixel width of 2.7 mm. Each 2D slice from a target-absent version (Fig. 1a) featured a centered circular disk with a 73-pixel radius, modeling homogeneous tracer uptake. A contrast-detail version of the phantom included 36 parallel rods extending axially, so that each phantom slice (Fig. 1b) displayed six rows of six circular targets apiece atop the circular background. The targets were spaced 17 pixels on center both vertically and horizontally. As shown in Fig. 1b, target radius varied left to right from 3.0 to 0.5 pixels in 0.5-pixel increments. From top to bottom, the target-to-background uptake ratio increased from 1.5 to 4.0 in increments of 0.5.

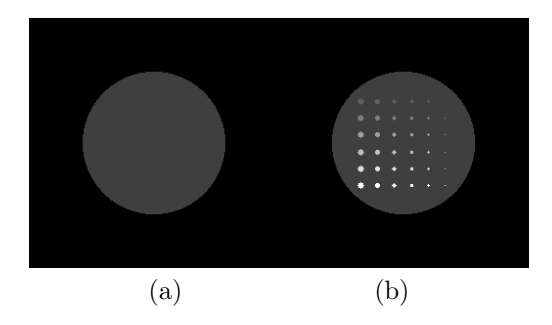


Figure 1. Single slices from the (a) homogeneous and (b) contrast-detail phantoms. In (b), the target-to-background uptake ratio increases from top to bottom in the 6×6 target grid, while target size decreases from left to right. Observer studies were performed at multiple quantum-noise levels for each of the 36 target positions.

An analytic projector included with the GE PET Reconstruction Toolbox⁹ was used to generate a set of noise-free projections from the phantoms. The projector included the effects of attenuation and variable system resolution. Photon scatter was modeled by combining these projections with a set of scaled projections obtained from blurred versions of the phantoms. The scatter and randoms fractions in the data were both set to 25%. Nine Poisson noise levels were defined by varying the total acquisition counts from 1200 M to 18.75 M, with the count levels varying by factors of two. In relative terms, the number of counts varied from 100% to approximately 0.4%. Time-of-flight measurements were not used in this study.

2.2 Image Reconstructions

Volume reconstructions with attenuation, scatter, and randoms correction were performed with the OSEM and HOTV iterative algorithms. The former is an accelerated version of the maximum-likelihood expectation-maximization (MLEM) algorithm which computes the reconstructed image f by minimizing the Poisson log likelihood objective function

$$L(f) = Hf - g \ln (Hf + \gamma). \tag{1}$$

In this equation, g is the projection data, H is the system projection matrix, and γ represents scatter and random counts. A well-known form of the MLEM update equation is 10

$$f^{k+1} = \frac{f^k}{H^t 1} H^t \left(\frac{g}{H f^k + \gamma} \right), \tag{2}$$

in which f^k is the k^{th} iterate, the superscript t represents a matrix transpose, and $\mathbf{1}$ is a vector of ones having the same dimension as g. However, an OSEM algorithm based on Eq. 2 does not converge. Instead, we used a proximal gradient algorithm that ensured ordered-sets convergence by means of a relaxation parameter.^{7,11}

The HOTV reconstructions minimized the penalized objective function

$$L(\mathbf{f}) + \lambda_1 \varphi_1(\mathbf{B}_1 \mathbf{f}) + \lambda_2 \varphi_2(\mathbf{B}_2 \mathbf{f}), \tag{3}$$

where matrices B_1 and B_2 respectively generate the first- and second-order discrete derivatives in f, functions φ_1 and φ_2 compute vector norms for these derivative images, and scalars λ_1 and λ_2 are the penalty weights.⁷ Here as well, a proximal gradient algorithm was applied with relaxation. The OSEM and HOTV reconstructions both used 15 iterations and 24 ordered subsets. These parameters, as well as the two HOTV penalty weights in Eq. 3, were preset based on methodology described by Schmidtlein *et al.*⁷

The HOTV reconstructions were not postfiltered, whereas the OSEM reconstructions were evaluated both with and without postfiltering. The processing consisted of a fixed three-point axial filter with kernel values [0.25,0.5,0.25], followed by transverse smoothing with a 2D Gaussian. The axial filter is well-suited for the 3D rod phantom in our simulation. Integer-valued Gaussian FWHMs over the range of [0,8] pixels were tested. An optimal FWHM for each of the nine count levels was determined by maximizing average observer performance over the 36 target locations.

With each of the eleven reconstruction strategies (HOTV, unfiltered OSEM, and nine postfiltered OSEM variants), 120 noisy volumes were obtained per phantom and count level. The center slice was extracted from each volume and preserved in floating-point format for use by the observer, for a total of 240 images per strategy and count level. Figure 2 presents low and high-count image examples from the contrast-detail phantom.

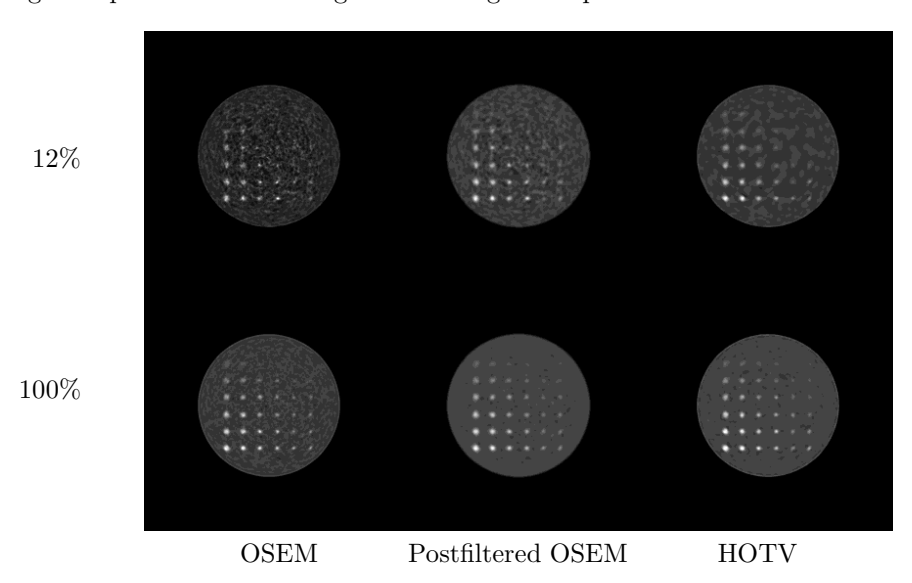


Figure 2. Sample test images. The top and bottom rows show low (12%) and high-count (100%) realizations, respectively, for the unfiltered OSEM, postfiltered OSEM (FWHM = 2 pixels), and HOTV strategies. The OSEM postsmoothing FWHM was optimized per count level for the observer study.

2.3 Model Observer

Overall, 324 location-known ROC studies (36 target locations and nine noise levels) were run with the reconstruction strategies. Performance was quantified in terms of the area under the ROC curve A_z . How a search-capable VS observer performs the location-known task has been described previously.¹² For a given test image, convolutional feature maps quantified correlations with target-like morphological features. Three difference-of-Gaussian (DOG) features corresponded to Gaussian blobs with sizes on the order of the target sizes in our study. Local maxima within a circular region of interest (ROI) in the three feature maps defined suspicious candidate locations, and the feature statistics at those locations were used as input to a statistical discriminant. A single ROI radius per strategy and count level was adaptively selected to optimize observer performance.

Each study used all available images for both training and testing. A relevant circular region about a given study location in the target-present and target-absent images was demarcated by a radius of nine pixels (see Fig. 3). This radius represented the maximum-allowed search ROI. To futher reduce intertarget interference with the contrast-detail phantom, we truncated the DOG functions outside of a seven-pixel radius. Note that the adaptive observer ROI that defined candidates was often two or three pixels in radius.

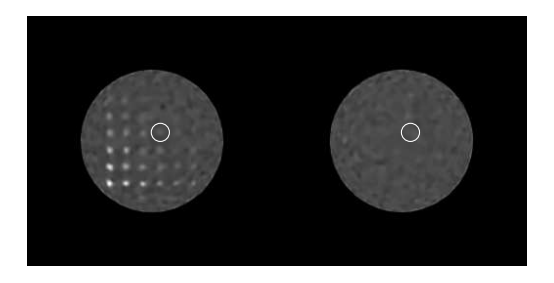


Figure 3. White circles with a nine-pixel radius denote the maximum-allowed search regions for the VS observer in target-present and target-absent cases for a given location-known study.

3. RESULTS

Figure 4 presents selected results from the OSEM postfilter optimization. Recall that all of the postfilter strategies applied axial smoothing. The plots show how observer performance at the 25% count level varied as a function of the transverse Gaussian FWHM for the upper-right quadrant of targets (indicated by the white box in the adjoining contrast-detail phantom). At this count level, transverse postfiltering had minimal impact with the relatively larger (left-hand plot column) and higher-uptake (lower row) targets. Only slight postfiltering was required with the remaining targets; larger FWHMs caused substantial reductions in A_z .

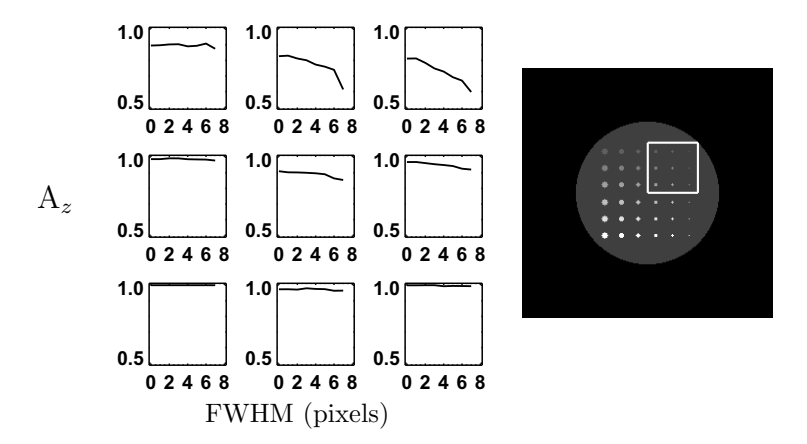


Figure 4. Results from the OSEM postfilter optimization. The plots show how observer performance at the 25% count level varied as a function of transverse Gaussian FWHM for the upper-right quadrant of targets indicated in the contrast-detail phantom.

The overall study results for the HOTV, unfiltered OSEM, and optimized OSEM (OSEM-opt) strategies are summarized in Fig. 5. Each contour plot shows how observer performance varied with respect to target size and uptake ratio for a given strategy and count level. The contours were formed on a 26×26 grid of A_z values interpolated from the original 6×6 grid of values obtained from the model observer. Each row of plots pertains to one strategy, with acquired counts decreasing from left to right. Within each plot, variations in uptake and size correspond to the phantom layout, with higher uptake and larger sizes in the bottom-left quadrant. A 10% grayscale was employed, with the brightest and darkest gray levels respectively representing A_z values of 1.0 and 0.5.

The interpolated A_z data used for Fig. 5 was distilled by computing the fractional area within each plot where A_z was at or above 0.95. This threshold was chosen as being clinically relevant. Figure 6 shows how this summary figure of merit varied with stategy and count level, indicating substantial differences between the HOTV and OSEM-opt strategies for relative count levels at or below 25%.

These differences were translated to physical imaging parameters through a psychometric analysis that related target phantom uptake to observer performance. Target uptake u was computed as the product of uptake ratio

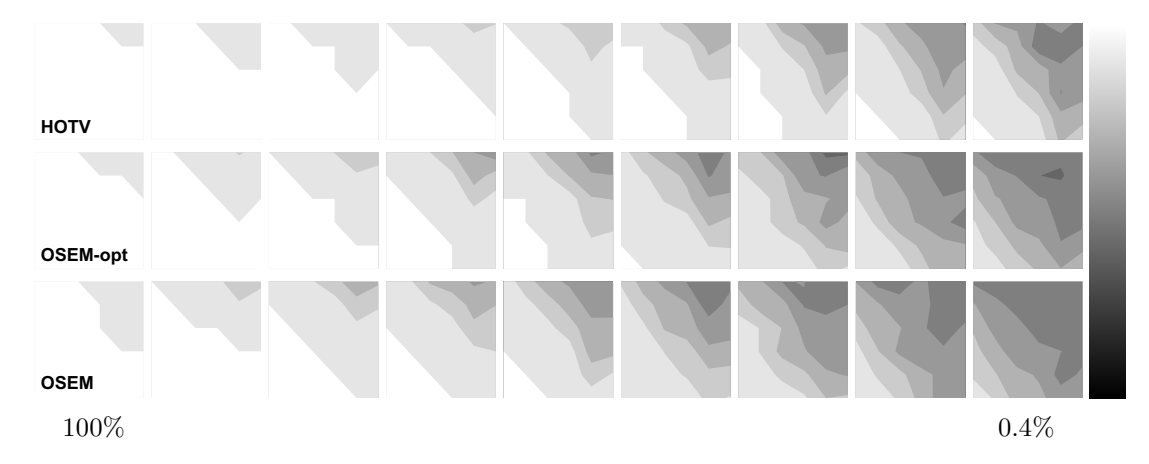


Figure 5. Summary of study outcomes. Each contour plot indicates how performance varied with target uptake and size for a given strategy and count level. Variations in uptake and size in a plot correspond with the contrast-detail phantom, with more conspicuous targets in the bottom-left quadrant. The lightest and darkest greyscales denote A_z values of 1.0 and 0.5 respectively. Acquired counts decrease by factors of two from 100% (left) to 0.4% (right).

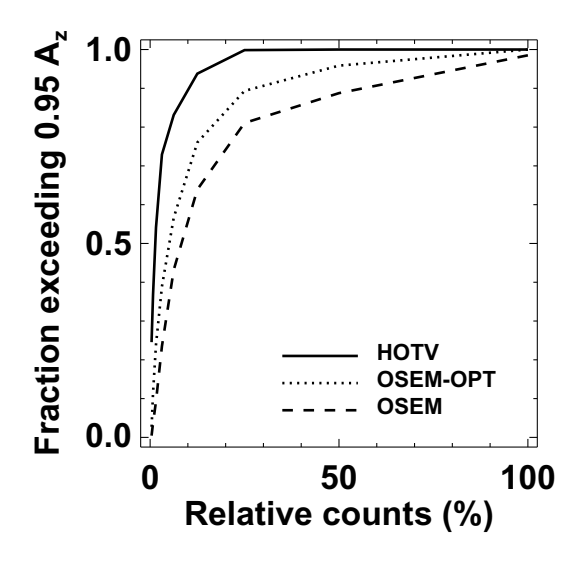


Figure 6. Fractional areas where $A_z \ge 0.95$ in the contour plots of Fig. 5.

and the squared target radius. Figure 7a presents a scatter plot of performance as a function of u for the HOTV strategy with 6% relative counts. Also shown is a logarithmic curve fit to the 36 data points. The threshold uptake required to attain $A_z = 0.95$ was estimated from this curve. Relatively unreliable estimates (or failure of the curve-fitting routine) occurred with some strategies at the highest and lowest count levels, where the observer operated entirely above or below the 0.95 threshold with all targets. Performing the analysis with uptake ratio and radius as independent variables could improve regression stability while accounting for partial-volume effects.

The log-log plot of Fig. 7b summarizes the psychometric results, showing how threshold uptake varied with count level for the three strategies. Over the count range from 3%–25%, unfiltered OSEM required uptakes nearly twice those of OSEM-opt to reach the performance threshold, while the latter strategy required uptakes slightly greater than twice those of the HOTV strategy. These numbers imply that HOTV permits a two-fold dose reduction for the task and observer applied in our studies.

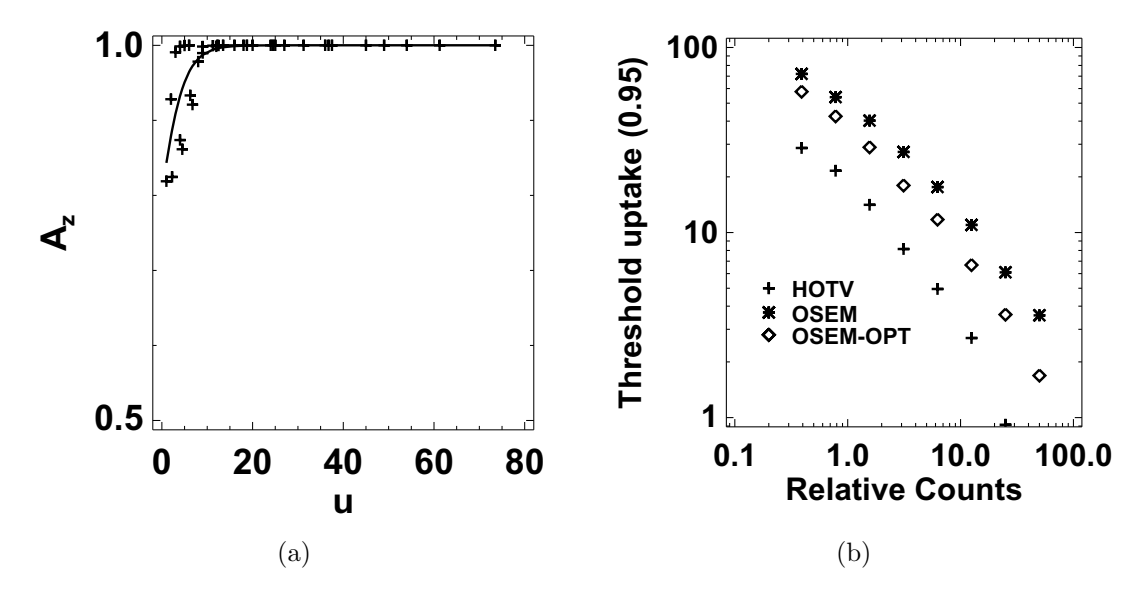


Figure 7. Psychometric analysis of performance as a function of target phantom uptake. (a) Scatter plot of performance as a function of target uptake u for the HOTV strategy with 6% relative counts. The solid line is a logarithmic curve fit to the data points. (b) A log-log plot showing threshold uptake variation with count level and reconstruction strategy.

4. CONCLUSIONS

We have conducted a preliminary task-based comparison of HOTV and postfiltered OSEM PET reconstruction algorithms, the latter of which is a clinical imaging standard. For location-known target detection, the HOTV algorithm allowed a two-fold dose reduction compared to the task-optimized OSEM algorithm. This work has also demonstrated the use of an anthropomorphic model observer to develop extensive preclinical psychometric data. Study limitations relate to possible intertarget correlations in the limited number of images. Future work will upgrade the clinical realism of the simulation and consider other penalized likelihood reconstruction algorithms.

5. ACKNOWLEDGMENTS

This research was supported in part by support/core grant P30-CA008748 from the Memorial Sloan Kettering Cancer Center and grant DMS-1912958 from the National Science Foundation.

REFERENCES

- 1. Y. Zhang, H. Hong, and W. Cai, "PET tracers based on Zirconium-89," *Current Radiopharmaceuticals*, vol. 4, pp. 131–139, 2011.
- M. Bourgeois, C. Bailly, M. Frindel, F. Guerard, M. Chérel, A. Faivre-Chauvet, F. Kraeber-Bodr, and C. Bodet-Milin, "Radioimmunoconjugates for treating cancer: recent advances and current opportunities," Expert Opinion on Biological Therapy, vol. 17, pp. 813–819, 2017.
- 3. M. A. Deri, B. M. Zeglis, L. C. Francesconi, and J. S. Lewis, "PET imaging with ⁸⁹Zr: from radiochemistry to the clinic," *Nuclear Medicine and Biology*, vol. 40, pp. 3–14, 2013.
- N. Pandit-Taskar, J. A. O'Donoghue, V. Beylergil, S. Lyashchenko, S. Ruan, S. B. Solomon, J. C. Durack, J. A. Carrasquillo, R. A. Lefkowitz, and M. Gonen, "89Zr-huJ591 immuno-PET imaging in patients with advanced metastatic prostate cancer," *European Journal of Nuclear Medicine and Molecular Imaging*, vol. 41, pp. 2093–105, 2014.
- B. Quinn, Z. Dauer, N. Pandit-Taskar, H. Schoder, and L. T. Dauer, "Radiation dosimetry of ¹⁸F-FDG PET/CT: incorporating exam-specific parameters in dose estimates," BMC Medical Imaging, vol. 16, p. 41, 2016.

- 6. N. Pandit-Taskar, J. A. O'Donoghue, S. Ruan, S. K. Lyashchenko, J. A. Carrasquillo, G. Heller, D. F. Martinez, S. M. Cheal, J. S. Lewis, and M. Fleisher, "First-in-human imaging with ⁸⁹Zr-Df-IAB2M anti-PSMA minibody in patients with metastatic prostate cancer: pharmacokinetics, biodistribution, dosimetry, and lesion uptake," *Journal of Nuclear Medicine*, vol. 57, pp. 1858–64, 2016.
- 7. C. R. Schmidtlein, Y. Lin, S. Li, A. Krol, B. J. Beattie, J. L. Humm, and Y. Xu, "Relaxed ordered subset preconditioned alternating projection algorithm for PET reconstruction with automated penalty weight selection," *Medical Physics*, vol. 44, pp. 4083–4097, 2017.
- 8. H. C. Gifford, "Visual-search observers for SPECT simulations with clinical backgrounds," *Proceedings of SPIE*, vol. 9787, 97870T, 2016.
- 9. S. Ross and K. Thielemans, General Electric PET Toolbox Release 2.0, 2005—2011.
- 10. H. M. Hudson and R. S. Larkin, "Accelerated image reconstruction using ordered subsets of projection data," *IEEE Transactions on Medical Imaging*, vol. 13, pp. 601–609, 1994.
- 11. S. Ahn and J. A. Fessler. "Globally convergent image reconstruction for emission tomography using relaxed ordered subsets algorithms." *IEEE Transactions on Medical Imaging*, vol. 22, pp. 613-626, 2003.
- 12. H. C. Gifford, Z. Karbaschi, K. Banerjee, and M. Das, "Visual search models for location-known detection tasks," *Proceedings of SPIE*, vol. 10136, 1013612, 2017.